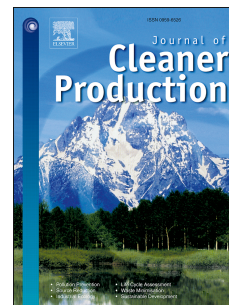# Accepted Manuscript

A new method to prepare mesoporous silica from coal gasification fine slag and its application in methylene blue adsorption

Shuo Liu, Xingtong Chen, Weidong Ai, Cundi Wei

Please cite this article as: Shuo Liu, Xingtong Chen, Weidong Ai, Cundi Wei, A new method to prepare mesoporous silica from coal gasification fine slag and its application in methylene blue adsorption, *Journal of Cleaner Production* (2018), doi: 10.1016/j.jclepro.2018.12.060

Object Images

TEM Images

FS

Solid Waste
Mass Production
High Silica Content

FS-MGS

Low Cost
Good Adsorptivity
Mesoporous Material

Sieving
Acid Leaching
600℃ Burning
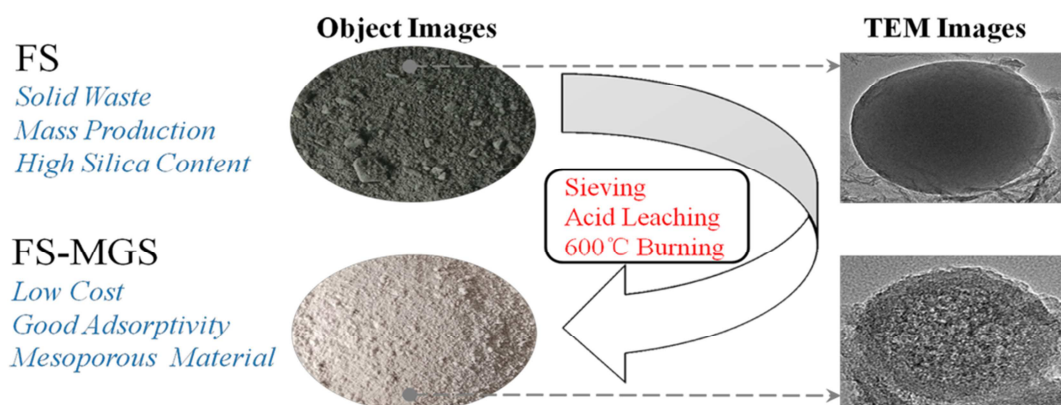
- Proposed a new method for large-scale production of mesoporous silica
- Prepared mesoporous silica with specific surface area of 364 m^2/g
- Prepared mesoporous silica with surface silanol content of 1.3 unit/nm^2
- Methylene blue maximum adsorption capacity of 140.57 mg/g

(word count: 7448)

A new method to prepare mesoporous silica from coal gasification fine slag and its application in methylene blue adsorption

Shuo Liu, Xingtong Chen, Weidong Ai, Cundi Wei*

Key Laboratory of Automobile Materials (Ministry of Education), College of Materials Science and

Engineering, Jilin University,

Changchun 130025, People's Republic of China

Abstract

Mesoporous silica materials are often restricted from large-scale industrial production due to their high preparation costs. This study used the solid waste coal gasification fine slag (FS) as the silica source, utilizing the simple acid leaching technology, successfully produced mesoporous glass microspheres (MGS) with specific surface area of 364 m^2/g and pore volume of 0.339 cm^3/g. The porous structure was confirmed by TEM. Moreover, the influences of reaction conditions on the specific surface area and pore structure were thoroughly investigated. The methylene blue adsorption test on the prepared mesoporous microspheres showed a maximum adsorption capacity of 140.57 mg/g. This research provides a new method for the industrial production of mesoporous silica.

Key Words: Coal gasification fine slag; Mesoporous glass microspheres; Acid leaching; Silanol group; Methylene blue adsorption

*Corresponding author: Tel.:+8618844198782; E-mail: weicundi_jlu@163.com

1. Introduction

Coal gasification slag (CGS) is a new type of solid waste produced from entrained-flow coal gasification (Rodney Andrews, 2006), which can be divided into coarse slag (CS, discharged from the lock hopper) and fine slag (FS, discharged by air flow) (Zhao et al., 2010). In China, around 700 various coal gasification furnaces were put into production and more than 250 million tons of coal was consumed in 2015 (Wang, 2016), and this number is increasing fleetly, so the annual output of CGS in China is hundreds of millions of tons. In order to achieve 'zero emission' of the coal gasification technology, it is necessary to find a way to utilize the waste. At present, many studies have explored the properties of unburned carbon in CGS (Wagner et al., 2008; Wu et al., 2014; Wu et al., 2007; Xu et al., 2009), but there is few research on the utilization of the silica in it. Some researchers have reported the physical and chemical properties of coal gasification slag. According to the different particle sizes, Pan et al. (Pan et al., 2016) reported basic properties of coal gasification slag, for example, composition, phase and pore structure. Zhao et al. (Zhao et al., 2010) discovered that the unburned carbon component in the fine slag existed as floccules and the various inorganic components existed as molten microspheres. Wu et al. (Wu et al., 2015) explored the elemental distribution of the molten inorganic microspheres in the fine slag. These studies shed light on the current research.

Since the initial preparation of mesoporous silica M41S by the Mobil Oil Company in 1992, various mesoporous silica materials have gained wide concerns in areas such as adsorption (Ali et al., 2018; Xu et al., 2018), catalysis (Dworakowska et al., 2017; Rahman et al., 2017), electrochemistry (Eftekhari, 2017; Mortazavi-Derazkola et al., 2017) and biosciences (Mortazavi-Derazkola et al., 2017; Sen and Bruce, 2009) due to their large specific surface area, ordered pore structure and abundant surface groups. Before that, the melting phase separation method was used to obtain porous glasses (Yazawa, 1995). This method melted inorganic powders such as SiO_2, Na_2O, and B_2O_3

to a glassy state at high temperature, and then leached out the metal oxides with acid to obtain the porous structure. Cao et al. (Cao et al., 2002) crushed the glass precursor (before acid leaching) into powder and sprayed it into a high-temperature zone where it melted instantly. Due to the surface tension effect, the molten droplets were cooled into microspheres, and the metal oxides were then leached out by acid to obtain mesoporous glass microspheres. Nevertheless, the above mentioned methods all incurred high production costs. In this research, the coal gasification fine slag microspheres was discovered to have various metal oxides naturally resided in them, similar to the products before the acid leaching process in the above method. These fine slag microspheres only required the acid leaching step to form a porous structure, which would greatly reduce the preparation cost.

So far, previous researches have reported the use of coal gasification slag to prepare mesoporous materials. Gu et al. (Gu and Qiao, 2018) used coal gasification slag as raw material, through KOH activation, formed a carbon silica composite material with a specific surface area of 1347 m^2g^{-1}. Li et al. (Li et al., 2016) used the fine slag from coal gasification as the silica source and prepared MCM-41 with uniform hexagonal pore shape and a specific surface area of 1347 m^2g^{-1} through the sol-gel method. However, both methods required high production cost and relatively complicated preparation processes, making it difficult to achieve large-scale industrial production. There were efforts trying to produce mesoporous materials from other inexpensive raw materials to reduce manufacturing cost (Bhattacharya and Mandal, 2018; Luo et al., 2017; Maroufi et al., 2017; Saygili and Guzel, 2016), however, the processes ended up with being costly as well because of the limitation of pore-forming technology. This study utilized the natural properties of coal gasification fine slag, through simple sieving, acid leaching and burning processes, successfully synthesized mesoporous glass microspheres with excellent adsorptivity and high thermal stability, which significantly reduced the preparation cost. So far, a variety of low cost materials are used for

decontamination (El-Korashy et al., 2016; Khalid Z.Elwakeel, 2017) ，and the material prepared in this study belongs to this category, which shows a excellent methylene blue adsorption capacity of 140.57 mg/g.Moreover, the current work provides a new way for the recycling of coal gasification solid waste, which will greatly benefit the environment.

2. Material and Methods

2.1 Raw Material

The main raw material was fine slag (FS), which was provided by Shenhua Ningxia Coal Industry Group Co., Ltd.. The samples for the experiments were prepared as follows: 100 g FS (with 55 wt% water) was diluted with water until the solid content was 20 wt%. At room temperature, the mixture was stirred using a high-speed dispersing stirrer at 1500 r/min for 40 minutes. The slurry was then introduced into a hydrocyclone separator, and the lower silicon-rich part was collected, sieved and dried to obtain FS1~FS6. The composition of FS3 is shown in Table 1 (provided by China Building Materials Industry Geological Exploration Center Jilin Corps Laboratory). The particle size distribution of FS1~FS6 is shown in Table 2 (measured by JL9200 laser particle size instrument).

2.2 Preparation and Characterization of Mesoporous Glass Microspheres

Under constant magnetic stirring (300 rpm), 10 g fine slag (particle size between FS1 and FS6) and 50 mL hydrochloric acid (concentration between 0 wt% and 20 wt%) were mixed in a flask. After 3 hours of stirring at room temperature, the mixture was filtered to obtain solids. The solids were washed with distilled water to remove residual ions in the pores and then dried at 120 °C for 12 h. Finally, the solids were burned in a Muffle Furnace at 600°C for 2 h to remove the carbon component and the FS-based mesoporous glass microspheres (FS-MGS) were obtained.

The pore structure of FS-MGS was characterized by nitrogen adsorption technique using a pore structure analyzer (JWGB Sci &Tech Ltd., China, JW-BK222). The specific surface area was determined using the (Brunauer-Emmett-Teller) BET equation and the pore size distribution was calculated using the Barrett-Joyner-Halenda (BJH) model. The phase composition of FS-MGS was analyzed by the X□ray diffractometer (China, DX-2700). Scanning electronic microscopy (Hitachi Ltd., Japan, TM4000) was used to observe the morphology of FS-MGS and transmission electron microscope (JEOL Ltd., Japan, JEM-F200) was used to observe the pore structure. Compositions of each sample were measured by China Building Materials Industry Geological Exploration Center Jilin Corps Laboratory. Metal oxide leaching rate was calculated according to equation (1):

$$\text{Leaching Rate(\%)} = \frac{m_0 - m}{m_0} \times 100\% \tag{1}$$

where m_0 (g) is the quantity of metal oxide in the sample before leaching; m (g) is the quantity of metal oxide in the sample after leaching.

2.3 Characterization of Surface Silanol Groups

The surface groups of FS-MGS were analyzed by the FTIR-650 Fourier transform infrared spectrometer to obtain the infrared diffuse reflection spectrum. The number of silanol groups was determined via acid-base titration method (Kang et al., 2001; Lin et al., 2009) : 2 g FS-MGS was added to 100 mL dilute sodium hydroxide solution (0.025 mol/L), and the mixture was magnetically stirred at room temperature for 12 h. After that, the mixture was filtered and two drops of phenolphthalein indicator were dripped into 20 mL filtrate. The filtrate was then titrated with dilute hydrochloric acid solution (0.025mol/L) until colorless. The amount of hydrochloric acid consumed was recorded as *A* (mL). Meanwhile, 20 mL same sodium hydroxide solution (0.025 mol/L) with two drops of phenolphthalein indicator was titrated with 0.025 mol/L hydrochloric acid solution until colorless, and the amount of hydrochloric acid consumed was recorded as *B* (mL). The content of surface hydroxy groups was calculated according to equations (2)

5

and (3):

$$X = \frac{(B - A) \times 0.025 \times 5}{2} \qquad (2)$$

where X (m mol/g) is the content of surface hydroxy groups per unit weight of FS-MGS.

$$N = (X \times N_A)/S \qquad (3)$$

where N (unit/nm^2) is the number of surface hydroxy groups per square nanometer of FS-MGS; N_A is the Avogadro constant; S (m^2/g) is the specific surface area of FS-MGS.

2.4 Methylene Blue Adsorption Test

Cationic Dye Methylene Blue (MB) was used as the absorbed media to test the adsorption properties of FS-MGS. The experimental process is as follows (Hor et al., 2016; Novais et al., 2018): First, 500 mg/L methylene blue solution was prepared and diluted to the desired concentration before the experiments. Adsorption tests were carried out in a series of Erlenmeyer flasks. About 0.1 g FS-MGS and 100 mL fresh methylene blue solution (concentration between 20-160 mg/L with 20 mg/L increment) were added to the flasks. The mixture was magnetically stirred for 24 h at room temperature for the reaction to reach equilibrium. The mixture was then centrifuged for 10 min at 15,000 rpm. After centrifugation, the methylene blue concentration in the supernatant solution was analyzed using a UV spectrophotometer (Beijing General Analysis Instrument Co., Ltd.，China, T6). The methylene blue absorbance change was measured at the wavelength of 665 nm, where absorbance was maximum. The amount of methylene blue absorbed by FS-MGS, Q_e (mg/g), was calculated according to equation (4):

$$Q_e = V(C_0 - C_e)/W \qquad (4)$$

where C_0 and C_e (mg/L) are the concentrations of MB in the liquid phase before reaction and at equilibrium, respectively; V (L) is the volume of methylene blue solution; and W (g) is the mass of dry FS-MGS.

The kinetics of the MB adsorption process was studied with 80 mg/L MB solution. The experiment was divided into 11 groups, and the reaction time of each group was 5 min, 10 min, 15 min, 20 min, 30 min, 40 min, 50 min, 60 min, 80 min, 100 min and 120 min, respectively. Other aspects of the experiment were same as the process described above. The amount of MB absorbed at time t, Q_t (mg/g) , was calculated by equation (5):

$$Q_t = V(C_0 - C_t)/W \tag{5}$$

where C_0 and C_t (mg/L) are the liquid-phase concentrations of MB in the beginning and at time t. V (L) is the volume of MB solution, and W (g) is the mass of FS1-MGS8 used.

For all regression analysis, the mean chi-square error (χ^2) analysis was performed, which was combined with the coefficient of determination (R^2) to prove the fit quality. The mean chi-square error was calcualted according to equation (6).

$$\chi^2 = \frac{1}{n}\sum\frac{(Q_{exp}-Q_{cal})^2}{Q_{cal}} \tag{6}$$

where, n is the number of data points; Q_{exp} is experimental data, and Q_{cal} is the calculated data using the regression equation.

3. Results and Discussion

3.1 Influence of Reaction Conditions on Pore Structure

It was found in the experiments that the main factors affecting the pore structure were acid concentration and fine slag (FS) particle size. With FS3 as raw material, the influence of acid concentration on pore structure and metal oxides leaching rates was studied. Table 3 shows the pore properties of FS-MGS formed under different acid concentrations, and the change of specific surface area with acid concentration is shown in Figure 1. It was found out that the relationship between specific surface area and acid concentration followed the Gaussian Model:

$$S = S_C + \frac{A}{\omega\sqrt{\pi/2}}\exp\left[-2(\frac{C-C_M}{\omega})^2\right] \tag{7}$$

where S (m^2/g) is the specific surface area of FS-MGS; S_C = -20.05, is the surface area

correction coefficient; A = 5197, is the peak area; ω = 14.66, is the peak width; and C_M = 16.15, is the acid concentration corresponding to the maximum specific surface area, which is the optimal acid concentration. The determination coefficient R^2 was 0.996 and the mean chi-square error χ^2 was 0.50，indicating a good fit between the Gaussian Model and experimental data.

The mechanism of pore formation in this research was the leaching of various metal oxides from the molten microspheres, creating pores at the locations where the original metal oxides resided. Two factors might affect the metal oxides leaching rate: acid concentration and/or metal oxides activity. Figure 2 shows the imapct of acid concentration on the leaching rate of several metal oxides. The experimental points were linked with solid lines to reflect the trend of change. With the increase of acid concentration, the changes of all metal oxides' leaching rates were similar (except for the more breakage of some Ca-O bonds at beginning), indicating metal oxides activity was not a major contributing factor to leaching rate. On the other hand, Figure 2 shows with the increase of acid concentration, the leaching rates of various metal oxides increased until reaching their own saturation value. This suggested leaching rate was positively correlated to acid concentration, and the ultimate leaching rate of the total metal oxides can reach 80%. Since the FS-MGS specific surface area was found to be dependent on acid concentration, it was thought that there would be a relationship between specific surface area and leaching rate, and according to Table 3, specific surface area and leaching rate were linearly correlated to each other, as is described by equation (8):

$$S = -10.94 + 312\gamma \ \ (R^2 = 0.98629, \chi^2 = 3.06) \tag{8}$$

where S (m^2/g) is the specific surface area of FS-MGS；γ (%) is the total leaching rate of all metal oxides.

The influence of acid concentration on average pore size of FS-MGS is shown in Table

3. The average pore size decreased with the increase of acid concentration. Pore size distribution of FS-MGS prepared with different acid concentrations is shown in Figure 3. When the acid concentration was low (FS3-MGS2), the pore size was distributed evenly within the range of 2~20 nm. As the acid concentration was increased, the number of large pores (pore size > 6 nm) did not change much, but the number of small pores (pore size between 2 and 6 nm) increased, contributing to the reduction of the average pore size. This indicated that the size of metal oxides resided in the FS-MGS sample glassy microspheres was mainly around 2~6nm. Thus there is a 2~6nm pore size distribution in microspheres after leaching out of the metal oxides.

The adsorption/desorption isotherms of FS-MGS samples prepared with different acid concentrations are shown in Figure 4. The adsorption capacity of all four samples increased with the increase of acid concentration, indicating that a higher porosity was achieved. Moreover, the slope of the adsorption/desorption loop was flatter at higher acid concentration. According to the type of adsorption/desorption loop defined by the de Boer model, as the acid concentration increases, the loop of the sample changes from type D to type B. However, the FS-MGS sample in this study originated from the leaching of various amorphous metal oxides, leading to the formation of pores of irregular shapes. Therefore, it is difficult to characterize the shape of pores according to the type of adsorption/desorption loop.

The influences of fine slag particle size on FS-MGS pore properties are shown in Table 4. Fine slags with particle sizes from FS1 to FS6 were used to prepare FS-MGS, and the optimal acid concentration (16.15 wt%) determined at the beginning of section 3.1 was applied. It can be seen from Table 4 that FS-MGS prepared with small FS particles showed larger specific surface area and pore volume than those prepared with large FS partiles; however, the FS particle size had negligible imapct on the pore size of the resultant FS-MGS. The mesoporous glass imcrosphere prepared in the current

9

experiment with the best pore properties was FS1-MGS8, which was used as the FS-MGS sample in the rest of the study.

3.2 FS1-MGS8 Composition and Phase

The composition of FS1-MGS8 is shown in Table 5. With FS1 as raw material, the leaching rate of metal oxides was the highest among all FS samples, giving rise to the largest specific surface area and pore volume of the resultant mesoporous glass microsphere. Note that, at 600 °C, there was still a small amount (3%) of unburned carbon present in the FS1-MGS8 sample.

Complex phase changes occur during coal gasification. For example, the kaolinite first transforms into metakaolin, and then transfroms into mullite (Mayoral et al., 2001); the quartz normally transforms into tridymite and cristobalite (Pan et al., 2016). Finally, at high temperature, lots of minerals melt into the glassy amorphous state (Mayoral et al., 2001). The amount of crystalline minerals in coal gasification slag is closely related to the area exposed. Small slag particles have relatively larger heated area and are easier to melt (Pan et al., 2016), thus lowering the amount of crystalline minerals present in the slag. The amorphous material used in the current study had high reactivity, which promoted the leaching of metal oxides from it. The XRD images of FS1-MGS8 is shown in Figure 5. The wide diffraction dispersion indicated a highly disordered structure in the sample. The existence of only one indistinct quartz diffraction peak in the spectrum suggested FS1-MGS8 was amorphous with tiny percentage of quartz phase.

3.3 Morphology

The Scanning Electron Microscope (SEM) images of raw material FS1 (a) and mesoporous glass microsphere FS1-MGS8 (b) are shown in Figure 6. Similar to what was reported by Zhao et al. (Zhao et al., 2010), FS1 consisted of molten spherical

inorganic mineral content (**S** in the figure) and flocculated unburned carbon content (**C** in the figure). The carbon content was burned to form the FS1-MGS8, which consisted only glass microspheres of uneven sizes. The diameters of the large spheres were in micron meters, while those of the small spheres were on nanoscale, aggregated into clusters. Wu et al. (Wu et al., 2015) reported that the coal gasification fine slag spheres with smooth surfaces were in a completely molten state and contained alkaline metal elements (Ca, Mg, Na, and K) of low melting points; the spheres with coarse surfaces were in a partially molten state and contained acidic metal elements (Al, Fe) of high melting points. The composition of the spheres determines the degree of melting. There was no sphere with coarse surface in FS1, so the inorganic content in the slag was in a completely molten state. However, the percentage of acidic metal elements in FS1 far exceeded the percentage of alkaline metal elements. This was probably due to the small particle size of FS1 giving rise to a relatively large heated area, which caused its complete melting during the gasification process. Therefore, the degree of melting of inorganic minerals in the coal gasification fine slags depends not only on their composition, but also on their particle sizes.

To further explore detailed information in morphology, a more advanced microscopy technique, Transmission Electron Microscopy (TEM), was applied instead of SEM to observe the pore structure of mesoporous glass microspheres. The TEM images of raw material FS1(a) and mesoporous glass microsphere FS1-MGS8 (b) are shown in Figure 7. It can be clearly seen that the sphere surface of raw material FS1 was very smooth and without pores. The molten microsphere with metal oxides leached out showed a highly porous surface, with the size of majority of the pores between 2 and 6 nm (Figure 4).

3.4 Surface Silanol Groups

The adsorption properties of siliceous materials are mainly determined by two aspects:

(1) the pore structure of silica; (2) surface chemical activity, which depends on the type and content of hydroxyl groups as well as the siloxane bridge. Therefore, the study of the surface silanol groups of FS1-MGS8 will help to fully understand its adsorption properties. Amorphous silica is a short-range ordered network with silica net of different sizes connected by Silicon-oxy tetrahedron. The various defects in the network make it easy for its surface "Si-O-"to combine with hydrogen to form surface silanol group. In an previous review article (Zhuravlev, 2000), L.T. Zhuravlev gave a very detailed report on the surface silanol groups of amorphous silicas. He suggested that the silanol groups could be classified into four types: (1) Isolated silanol groups，$\equiv$SiOH; (2) Geminal silanol groups，$=$Si(OH)$_2$; (3) Vicinal silanol groups (containing hydrogen bond) and (4) Internal silanol groups (not discussed). Furthermore, the Vicinal silanol groups completely disappeared before 400 °C. Between 400 and 900 °C, only Isolated silanol groups and Geminal silanol groups remained in amorphous silica (Zhuravlev, 2000). After subjecting to the burning temperature of 600 °C in the preparation process of this work, FS1-MGS8 was expected to have its silanol type of Isolated silanol and Geminal silanol. M.A. Al-Ghouti et al. (Al-Ghouti et al., 2003) reported that in the infrared spectrum of diatomite, the silanol group vibration peaks were around 3700 cm^{-1}. P. Yuan et al. (Yuan et al., 2004; Yuan et al., 2001) reported the diffuse reflection infrared peaks of diatomite surface hydroxyl groups were between 3000 and 4000 cm^{-1}. He pointed out that silanols with strong hydrogen bonds combined with water molecules could produce a wide vibration peak below 3500 cm^{-1}, and these silanols were more likely to condense to form the siloxane bridge as temperature was increased. The diffuse reflection Fourier transform infrared spectrum of FS1-MGS8 between 3000~4000 cm^{-1} is shown in Figure 8. Its characteristic peaks were mainly shown between 3500~3750 cm^{-1}, and there was no wide characteristic peak between 3000~3500 cm^{-1}. This suggested there was no strong hydrogen bond in the FS1-MGS8 silanol groups. In addition, P. Yuan (Yuan et al., 2004) reported that the silanol groups associated with weak hydrogen bonds in diatomite showed a weak vibration peak at 3740 cm^{-1}, which became more obvious as

temperature was increased. The spectrum of FS1-MGS8 around 3740 cm^{-1} was relatively smooth, indicating there was no weak hydrogen bond in the FS1-MGS8 silanol groups either. According to the above analysis, it can be concluded that the main types of surface silanol groups in FS1-MGS8 are Isolated and Genimal silanols (schematic diagram is shown in Figure 9). However, it is not excluded that tiny amount of Vicinal silanols may exist in the fine pores.

The silanol content in FS1-MGS8 after calcination at 600~1100□ is shown in Figure 10. Before 1000 °C, the silanol content decreased with the increase of calcination temperature. The Genimal silanol groups disappeared first, followed by the missing of the Isolated silanol groups. Finally only the siloxane bridge was left (Zhuravlev, 2000). The presence of 'silanol' in FS1-MGS8 after calcination at 1000°C and 1100°C was probably due to the reaction of small amount of NaOH with non-Si-OH species (Al$_2$O$_3$, SiO$_2$) during the test. So the actual silanol content in FS1-MGS8 was:

$$X=0.5625-0.0438=0.5187 \text{ (m mol/g)} \tag{9}$$

$$N=1.31-0.1=1.3 \text{ (unit/nm}^2) \tag{10}$$

where *X* is the content of surface silanol groups per unit weight of FS-MGS; *N* is the number of surface silanol groups per square nanometer of FS-MGS.

3.5 Methylene Blue Adsorption Behavior of FS1-MGS8

Methylene blue (MB) is a type of cationic dye which is widely used in textile, printing, leather and other industries. Due to its strong adsorbability to solids, MB is often used as an indicator of solid adsorption capacity (Zhang et al., 2013). The adsorption isotherm of MB (initial pH value was between 7.30 ~ 7.88) onto FS1-MGS8 at room temperature (20°C) is shown in Figure 11. In the beginning, the equilibrium adsorption capacity was low due to the limitation of the low MB concentration in the solution. As the MB concentration was increased, the equilibrium adsorption capacity increased until approaching a saturation value. The increase in equilibrium adsorption capacity was

13

resulted from the increment of adsorption driving force, *i.e.* concentration gradient. When the MB concentration was high, the active adsorption sites in FS1-MGS8 were surrounded by more MB ions, and at equilibrium, more adsorption sites were occupied by the MB ions (Yao et al., 2010). As all the active adsorption sites in FS1-MGS8 were occupied, further increment in MB concentration would not contribute to the adsorption of more MB ions and thus the maximum adsorption capacity was reached.

Adsorption isotherms describe the interaction between adsorbent and adsorbate. In order to characterize the distribution of MB on the surface of FS1-MGS8 at equilibrium, the widely used Freundlich Model (Freundlich, 1932) and Langmuir Model (Langmuir, 1916) were adopted in the current work to fit experimental data, as is shown in Figure 11. The linear expression of the two adsorption models is shown in equations (11) and (12) :

Freundlich Model:

$$Q_e = K_F C_e^{\frac{1}{n}} \tag{11}$$

where K_F and n are related to adsorption capacity and adsorption intensity of the system.

Langmuir Model:

$$Q_e = \frac{Q_{m,L} K_L C_e}{1 + K_L C_e} \tag{12}$$

where Q_m is the maximum adsorption capacity; K_L is a Langmuir constant related to the affinity of the binding sites and energy of adsorption.

Figure 11 shows the fitting of experimental data to the Freundlich and Langmuir models, and the corresponding parameters are given in Table 6. By comparison, the experimental data fitted the Langumir Model better than the Freundlich Model, which was also supported by the high coefficient of determination (R^2=0.991) and small mean chi-square error (χ^2=0.12) of the Langmuir Model fitting. According to the occurrence conditions of Langmuir Model, MB molecules are monolayer covering on the surface of FS1-MGS8, *i.e.*, one MB molecule occupies only one adsorption site. As indicated in Table 6, the maximum adsorption capacity of MB onto FS1-MGS8 was 140.57 mg/g at room temperature. In a review article written by Rafatullah et al. (Rafatullah et al.,

2010), more than 180 kinds of low-cost methylene blue adsorbents were reported, including various activated carbons, siliceous materials, natural materials and processed wastes. Among them, activated carbons showed relatively higher adsorption capacity, which was in the range of 0.84 ~ 980 mg/g; and the siliceous materials were the second best, which showed MB adsorption capacity of 2.24 ~ 300 mg/g. For the FS1-MGS8 prepared in the current work, its MB adsorption capacity is higher than 50 percent of the activated carbons and 80 percent of the siliceous materials reported by Rafatullah. Moreover, the high preparation cost and the complicated processes limited the application of the materials reported in Rafatullah's article, which made the results obtained in the current work important for industrial application.

To understand the kinetics of MB dyes adsorption onto FS1-MGS8, experimental data was fitted to three kinetic models: the pseudo first-order model，pseudo second-order model and Weber & Morris model. The expressions of the three kinetic models are as follows.

Pseudo first-order model: $$Q_t = Q_e(1 - e^{-K_1 t}) \tag{13}$$

Pesudo second-order model: $$Q_t = \frac{K_2 Q_e^2 t}{1 + K_2 Q_e t} \tag{14}$$

Weber & Morris model: $$Q_t = K_i t^{\frac{1}{2}} + C \tag{15}$$

where K_1 is the first-order adsorption rate constant; K_2 is the second-order adsorption rate constant, and K_i is the intra-particle diffusion rate constant.

Figure 12 shows the fitting of experimental data to the three kinetic models, and the corresponding kinetic parameters are given in Table 7. By comparison, it can be seen that experimental data fitted the pseudo second-order model the best, as was supported by its high R^2 and small χ^2. The good fitting to the pseudo second-order model indicated that the mechanism for the adsorption of MB onto FS1-MGS8 was chemical adsorption, which involved electrostatic interaction between the surface charge of FS1-MGS8 and MB^+ (Elwakeel and Al-Bogami, 2018). The fitting to the Weber & Morris model also looked good (Figure 12b). The first linear section was a steep slope, suggesting rapid adsorption in the beginning; while the second linear section was a flat slope, indicating slow adsorption in the end when the process was approaching equilibrium. The linear plot didn't pass through the origin, suggesting that the resistance

to intra-particle diffusion is not the sole rate-limiting factors. Other steps, for example, resistance to film diffusion and/or reaction rate, were probably involved in the control of uptake kinetics (K.Z.Elwakeel, 2017) .

The Fourier-Transform Infrared Spectroscopy (FTIR) spectrum of FS1-MGS8 before and after methylene blue adsorption is shown in Figure 13. This spectrum is similar to another amorphous silica reported by Yuan and Zhi, the $SiO_2 \cdot nH_2O$ (Yuan et al., 2014; Zhi and Guo, 2013). In figure 13, the small peak at 960.76 cm^{-1} corresponds to the Si-O-H vibration, which disappeared after adsorption of MB. This result indicated that the H$^+$ was ionized out in the MB solution, and an electrostatic attraction was probably formed between [SiO]$^-$ and MB$^+$. In addition, the strength of the Si-O-Si vibration peaks at 1087.55 cm^{-1}, 794.65 cm^{-1} and 466.39cm^{-1} decreased after adsorption, which was probably due to the coverage of FS1-MGS8 by the MB molecules that reduced the Si-O-Si bond's transmittance. On the other hand, the strength of the H-O-H vibration peaks at 1398.99 cm^{-1}, 1634.79 cm^{-1} and 3444.36 cm^{-1} increased after adsorption, which was probably contributed by the adsorption of H$_2$O molecules carried by the MB solution.

Possible adsorption mechanism is as follows. The adsorption capacity of solid materials depends not only on the specific surface area and pore structure, but also on the surface properties. For adsorption onto solid surface, six mechanisms might exist (*i.e.*, electrostatic interaction, ion exchange, ion–dipole interactions, coordination by surface metal cations, hydrogen-bonding and hydrophobic interaction) (Liu et al., 2013). In the case of MB adsorption onto FS1-MGS8, we believe the electrostatic interaction plays an important role. Specifically, the H$^+$ dissociates from the surface silanol group of FS1-MGS8 to generate [SiO]$^-$, which will form electrostatic attraction with the cationic MB$^+$. The pH of the MB solution is an important influencing factor for the adsorption of MB onto FS1-MGS8. In acidic environment, the FS1-MGS8 surface is surrounded by the positively charged H$^+$, which tends to prevent the adsorption of the cationic MB$^+$

16

due to ionic repulsion. When pH of the MB solution is increased, the FS1-MGS8 surface is more negatively charged, and an increase in the adsorption of MB^+ is expected since the ionic repulsion will be weakened and the electrostatic attraction between the positively charged MB^+ and negatively charged FS1-MGS8 will be strengthened. The impact of pH on the adsorption of MB onto FS1-MGS8 is shown in Table 8. The adsorption capacity increased with the increase of pH value, which supported the above argument. On the other hand, under acidic conditions, FS1-MGS8 still showed good adsorption of MB. This might be due to the formation of hydrogen bonds between the surface silanol group of MS1-MGS8 and the nitrogen atom in MB (Al-Ghouti et al., 2003). Therefore, the adsorption mechanism of MB onto MS1-MGS8 is probably a combination of electrostatic interaction and hydrogen-bonding. The two adsorption mechanisms are shown in Figure 14.

4. Conclusions

This study proposed a low-cost method for the preparation of mesoporous glass microsphere using the natural properties of coal gasification fine slags. It not only provided a method for the industrial production of mesoporous silica, but also found a new direction for the utilization of coal gasification slag waste. The main findings of this research are:

(1) The relationship between the specific surface area of the mesoporous glass microsphere and the acid concentration follows the Gaussian model; the relationship between specific surface area and leaching rate follows a one-dimensional linear model. The specific surface area of the mesoporous glass microsphere is negatively correlated to the particle size of the coal gasification slag. Under the optimal reaction conditions, mesoporous glass microsphere FS1-MGS8 with a specific surface area of 364 m^2/g, pore volume of 0.339 cm^3/g, and pore size mainly distributed between 2 and 6 nm were prepared.

(2) The main types of surface silanol groups on FS1-MGS8 are Isolated silanol groups

and Genimal silanol groups, and the content of silanol groups is 1.3 unit/nm^2.

(3) The maximum adsorption capacity of methylene blue onto FS1-MGS8 was 140.57 mg/g. The adsorption isotherm was best described by the Langumir model, and the adsorption kinetics was best described by the pseudo-second order kinetic model. The adsorption mechanism is a combination of electrostatic interaction and hydrogen-bonding.

References

Al-Ghouti, M.A., Khraisheh, M.A.M., Allen, S.J., Ahmad, M.N., 2003. The removal of dyes from textile wastewater: a study of the physical characteristics and adsorption mechanisms of diatomaceous earth. Journal Of Environmental Management 69, 229-238.

Ali, M.M.M., Ahmed, M.J., Hameed, B.H., 2018. NaY zeolite from wheat (Triticum aestivum L.) straw ash used for the adsorption of tetracycline. Journal Of Cleaner Production 172, 602-608.

Bhattacharya, M., Mandal, M.K., 2018. Synthesis of rice straw extracted nano-silica-composite membrane for CO2 separation. Journal Of Cleaner Production 186, 241-252.

Cao, Z., Zhang, X., Wang, W., Wang, X., Zhao, Z., Wang, J., 2002. Preparation and adsorption properties of porous glass microspheres. Journal of the Chinese Ceramic Society 30, 402-406.

Dworakowska, S., Tiozzo, C., Niemczyk-Wrzeszcz, M., Michorczyk, P., Ravasio, N., Psaro, R., Bogdal, D., Guidotti, M., 2017. Mesoporous molecular sieves containing niobium (V) as catalysts for the epoxidation of fatty acid methyl esters and rapeseed oil. Journal Of Cleaner Production 166, 901-909.

Eftekhari, A., 2017. Ordered mesoporous materials for lithium-ion batteries.

Microporous And Mesoporous Materials 243, 355-369.

El-Korashy, S.A., Elwakeel, K.Z., Abd El-Hafeiz, A., 2016. Fabrication of bentonite/thiourea-formaldehyde composite material for Pb (II), Mn (VII) and Cr (VI) sorption: A combined basic study and industrial application. Journal Of Cleaner Production 137, 40-50.

Elwakeel, K.Z., Al-Bogami, A.S., 2018. Influence of Mo(VI) immobilization and temperature on As(V) sorption onto magnetic separable poly p-phenylenediamine-thiourea-formaldehyde polymer. Journal Of Hazardous Materials 342, 335-346.

Freundlich, H., 1932. H. Freundlich Of the adsorption of gases. Section II. Kinetics and energetics of gas adsorption. Introductory paper to section II. Transactions of the Faraday Society 38, 0195-0201.

Gu, Y.-y., Qiao, X.-c., 2018. A carbon silica composite prepared from water slurry coal gasification slag. Microporous and Mesoporous Materials.

Hor, K.Y., Chee, J.M.C., Chong, M.N., Jin, B., Saint, C., Poh, P.E., Aryal, R., 2016. Evaluation of physicochemical methods in enhancing the adsorption performance of natural zeolite as low-cost adsorbent of methylene blue dye from wastewater. Journal Of Cleaner Production 118, 197-209.

Kang, S., Hong, S.I., Choe, C.R., Park, M., Rim, S., Kim, J., 2001. Preparation and characterization of epoxy composites filled with functionalized nanosilica particles obtained via sol-gel process. Polymer 42, 879-887.

K.Z.Elwakeel, A.A.E.-B., E.Y.Kouta, 2017. Retention of copper, cadmium and lead from water by Na-Y-Zeolite confined in methyl methacrylate shell. Journal of Environmental Chemical Engineering 5, 3698-3710.

Khalid Z.Elwakeel, A.M.E., Samya H.Mohammad, 2017. Use of beach bivalve shells located at Port Said coast (Egypt) as a green approach for methylene blue removal. Journal of Environmental Chemical Engineering 5, 578-587.

Langmuir, I., 1916. THE CONSTITUTION AND FUNDAMENTAL PROPERTIES OF SOLIDS AND LIQUIDS. PART I. SOLIDS. Journal of the American Chemical Society 38, 2221-2295.

Li, C.-c., Qiao, X.-c., Yu, J.-g., 2016. Large surface area MCM-41 prepared from acid leaching residue of coal gasification slag. Materials Letters 167, 246-249.

Lin, O.H., Akil, H.M., Ishak, Z.A.M., 2009. Characterization and Properties of Activated Nanosilica/Polypropylene Composites With Coupling Agents. Polymer Composites 30, 1693-1700.

Liu, M., Hou, L.-a., Xi, B., Zhao, Y., Xia, X., 2013. Synthesis, characterization, and mercury adsorption properties of hybrid mesoporous aluminosilicate sieve prepared with fly ash. Applied Surface Science 273, 706-716.

Luo, H., Wu, Y., Zhao, A., Kumar, A., Liu, Y., Cao, B., Yang, E.-H., 2017. Hydrothermally synthesized porous materials from municipal solid waste incineration bottom ash and their interfacial interactions with chloroaromatic compounds. Journal Of Cleaner Production 162, 411-419.

Maroufi, S., Mayyas, M., Sahajwalla, V., 2017. Waste materials conversion into mesoporous silicon carbide nanocermics: Nanofibre/particle mixture. Journal Of Cleaner Production 157, 213-221.

Mayoral, M.C., Izquierdo, M.T., Andres, J.M., Rubio, B., 2001. Aluminosilicates transformations in combustion followed by DSC. Thermochimica Acta 373, 173-180.

Mortazavi-Derazkola, S., Salavati-Niasari, M., Khojasteh, H., Amiri, O., Ghoreishi, S.M., 2017. Green synthesis of magnetic Fe3O4/SiO2/HAp nanocomposite for atenolol delivery and in vivo toxicity study. Journal Of Cleaner Production 168, 39-50.

Novais, R.M., Ascensao, G., Tobaldi, D.M., Seabra, M.P., Labrincha, J.A., 2018. Biomass fly ash geopolymer monoliths for effective methylene blue removal from wastewaters. Journal Of Cleaner Production 171, 783-794.

Pan, C., Liang, Q., Guo, X., Dai, Z., Liu, H., Gong, X., 2016. Characteristics of Different Sized Slag Particles from Entrained-Flow Coal Gasification. Energy & Fuels 30, 1487-1495.

Rafatullah, M., Sulaiman, O., Hashim, R., Ahmad, A., 2010. Adsorption of methylene blue on low-cost adsorbents: A review. Journal Of Hazardous Materials 177, 70-80.

Rahman, A.F.A., Jalil, A.A., Triwahyono, S., Ripin, A., Aziz, F.F.A., Fatah, N.A.A., Jaafar, N.F., Hitam, C.N.C., Salleh, N.F.M., Hassan, N.S., 2017. Strategies for introducing titania onto mesostructured silica nanoparticles targeting enhanced photocatalytic activity of visible-light-responsive Ti-MSN catalysts. Journal Of Cleaner Production 143, 948-959.

Rodney Andrews, A.R., Jack Groppo, Brock Marrs, Ari Geertsema, Frank Huggins, M. Mercedes Maroto-Valer, Brandie M. Markley, Zhe Lu, and Harold Schobert, 2006.

Advanced Gasification By-Product Utilization. . In: Nineteenth Pittsburgh Coal Conference.

Saygili, H., Guzel, F., 2016. High surface area mesoporous activated carbon from tomato processing solid waste by zinc chloride activation: process optimization, characterization and dyes adsorption. Journal Of Cleaner Production 113, 995-1004.

Sen, T., Bruce, I.J., 2009. Mesoporous silica-magnetite nanocomposites: Fabrication, characterisation and applications in biosciences. Microporous And Mesoporous Materials 120, 246-251.

Wagner, N.J., Matjie, R.H., Slaghuis, J.H., van Heerden, J.H.P., 2008. Characterization of unburned carbon present in coarse gasification ash. Fuel 87, 683-691.

Wang, S., 2016. Development and applicatin of modern coal gasification technology. CHEMICAL INDUSTRY AND ENGINEERING PROGRESS 35, 653-664.

Wu, S., Huang, S., Ji, L., Wu, Y., Gao, J., 2014. Structure characteristics and gasification activity of residual carbon from entrained-flow coal gasification slag. Fuel 122, 67-75.

Wu, S., Huang, S., Wu, Y., Gao, J., 2015. Characteristics and catalytic actions of inorganic constituents from entrained-flow coal gasification slag. Journal Of the Energy Institute 88, 93-103.

Wu, T., Gong, M., Lester, E., Wang, F., Zhou, Z., Yu, Z., 2007. Characterisation of residual carbon from entrained-bed coal water slurry gasifiers. Fuel 86, 972-982.

Xu, S., Zhou, Z., Gao, X., Yu, G., Gong, X., 2009. The gasification reactivity of unburned carbon present in gasification slag from entrained-flow gasifier. Fuel Processing Technology 90, 1062-1070.

Xu, X., Li, Y., Yang, D., Zheng, X., Wang, Y., Pan, J., Zhang, T., Xu, J., Qiu, F., Yan, Y., Li, C., 2018. A facile strategy toward ion-imprinted hierarchical mesoporous material via dual-template method for simultaneous selective extraction of lithium and rubidium. Journal Of Cleaner Production 171, 264-274.

Yao, Y., Xu, F., Chen, M., Xu, Z., Zhu, Z., 2010. Adsorption behavior of methylene blue on carbon nanotubes. Bioresource Technology 101, 3040-3046.

Yazawa, T., 1995. Present Status and Future Potential of Preparation of Porous Glass and its Applications. Key Engineering Materials 115, 125-146.

Yuan, P., Wu, D.Q., He, H.P., Lin, Z.Y., 2004. The hydroxyl species and acid sites on diatomite surface: a combined IR and Raman study. Applied Surface Science 227, 30-39.

Yuan, P., Wu, D.Q., Lin, Z.Y., Diao, Q.Y., Peng, J.L., Wei, J.F., 2001. Study on the surface hydroxyl of diatomite by diffuse reflectance infrared spectroscopy (DRIFT). Spectroscopy and Spectral Analysis 21, 783-786.

Yuan, W., Yao, Z., Zhang, Q., Li, J., 2014. Characterization of residue from leached cathode ray tube funnel glass: reutilization as white carbon black. Journal Of Material Cycles And Waste Management 16, 629-634.

Zhang, J., Ping, Q., Niu, M., Shi, H., Li, N., 2013. Kinetics and equilibrium studies from the methylene blue adsorption on diatomite treated with sodium hydroxide. Applied Clay Science 83-84, 12-16.

Zhao, X., Zeng, C., Mao, Y., Li, W., Peng, Y., Wang, T., Eiteneer, B., Zamansky, V., Fletcher, T., 2010. The Surface Characteristics and Reactivity of Residual Carbon in Coal Gasification Slag. Energy & Fuels 24, 91-94.

Zhi, X., Guo, Z., 2013. Study on the Preparing of Nano White Carbon Black by Silica Fume, in: Zheng, L., Skuroda, S., Liu, H., Du, B., Wei, J., Zhao, Y. (Eds.), Applied Materials And Technologies for Modern Manufacturing, Pts 1-4, pp. 554-+.

Zhuravlev, L.T., 2000. The surface chemistry of amorphous silica. Zhuravlev model. Colloids And Surfaces a-Physicochemical And Engineering Aspects 173, 1-38.

Tables

Table 1 Chemical composition of FS3 (wt %)

SiO_2	Al_2O_3	CaO	Fe_2O_3	Na_2O	K_2O	MgO	Ti_2O	L.O.I	Others
43.09	19.23	8.20	6.39	2.72	1.75	0.84	0.95	15.18	1.83

Table 2 Partical size distribution of FS1~FS6

Sample	D_{av} (µm)	D_{10} (µm)	D_{50} (µm)	D_{90} (µm)
FS1	6.265	1.089	4.953	13.344
FS2	7.266	1.316	5.821	15.329
FS3	9.965	1.435	7.489	22.003
FS4	11.794	1.671	8.838	26.032
FS5	13.563	2.167	10.538	29.252
FS6	19.620	2.351	14.005	44.447

*D_{10}, 10% of particles have a particle size below D_{10} ; *D_{50}, 50% of the particles have a particle size below D_{50} ; *D_{90}, 90% of the particles have a particle size below D_{90} ;* D_{av}, the average particle size.

Table 3 The pore properties of FS3-MGS under different reactive conditions

Sample	Acid concentration (%)	Total leaching rate (%)	Specific surface area (m^2/g)	Pore volume (cm^3/g)	Average pore size (nm)
FS3-MGS0	0	0	5	0.032	10.732
FS3-MGS1	2	10	21	0.061	10.012
FS3-MGS2	4	21	43	0.128	9.641
FS3-MGS3	6	30	102	0.211	7.132
FS3-MGS4	8	50	134	0.240	7.541
FS3-MGS5	10	65	177	0.232	6.622
FS3-MGS6	12	76	224	0.242	5.409
FS3-MGS7	14	80	259	0.264	5.292
FS3-MGS8	16	80	252	0.232	4.634
FS3-MGS9	18	79	246	0.259	4.973
FS3-MGS10	20	79	236	0.270	5.224

Table 4 The pore properties of FS-MGS8 formed from different raw materials

Sample	D_{av} (µm)	Specific surface area (m^2/g)	Pore volume (cm^3/g)	Average pore size (nm)
FS1-MGS8	6.265	364	0.339	4.732
FS2-MGS8	7.266	303	0.275	4.688
FS3-MGS8	9.965	253	0.232	4.634
FS4-MGS8	11.794	226	0.196	4.511
FS5-MGS8	13.563	180	0.168	4.689
FS6-MGS8	19.260	153	0.155	5.049

Table 5 Chemical composition of FS1-MGS8 (wt %)

SiO_2	Al_2O_3	CaO	Fe_2O_3	Na_2O	K_2O	MgO	Ti_2O	L.O.I	Others
88.77	4.56	0.63	0.81	0.49	0.35	0.12	0.60	2.96	0.71

Table 6 Equilibrium model fitting parameters for the adsorption of MB onto FS1-MGS8

Freundlich	n	K_F (mg/g)	R^2	χ^2
	3.18	53.36	0.939	2.21

Langmuir	$Q_{m,L}$ (mg/g)	K_L (L/mg)	R^2	χ^2
	140.57	0.54	0.991	0.12

Table 7 Kinetic model fitting parameters for the adsorption of MB onto FS1-MGS8

Pseudo first order		$Q_{e, cal}$ (mg/g)	K_1 (min^{-1})	R^2	χ^2
		76.53	0.34	0.820	0.038
Pseudo second order		$Q_{e, cal}$ (mg/g)	K_2 (g mg^{-1} min^{-1})	R^2	χ^2
		78.70	0.011	0.995	0.0015
Weber and Morris	Part I	C	K_i (mg g^{-1} min$^{0.5}$)	R^2	χ^2
		53.85	4.94	0.941	0.0094
	Part II	C	K_i (mg g^{-1} min$^{0.5}$)	R^2	χ^2
		75.42	0.243	0.855	0.0025

Table 8 Maximum Langmuir adsorption capacity of methylene blue onto FS1-MGS8 under different pH values

Initial pH	3	4	5	6	7	8	9	10
Equilibrium pH	3.12	4.32	5.55	6.08	6.13	6.42	6.79	7.115
$Q_{m,L}$(mg/g)	119.13	125.92	133.60	136.66	138.08	141.17	146.30	150.73

Figure captions

Figure 1 Fitting of FS3-MGS BET specific surface area to the Gaussian model.

Figure 2 Impacts of acid concentration on the leaching rate of various metal oxides.

Figure 3 BJH desorption pore size distribution of FS3-MGS2, FS3-MGS4, FS3-MGS6 and FS3-MGS8. The acid concentration used in the preparation of the samples was 4 wt%, 8 wt%, 12 wt% and 16 wt%, respectively.

Figure 4 The N-adsorption/desorption isotherms of FS3-MGS2, FS3-MGS4, FS3-MGS6 and FS3-MGS8. The acid concentration used in the preparation of the samples was 4 wt%, 8 wt%, 12 wt%, 16 wt%, respectively.

Figure 5 XRD spectrum of FS1-MGS8.

Figure 6 The SEM images of raw material FS1 (a) and mesoporous glass microsphere FS1-MGS8 (b). The bright parts labelled with C are focculated unburned carbon content; the gray parts labelled with S are molten spherical inorganic mineral content.

Figure 7 The TEM images of raw material FS1 (a) and mesoporous glass microsphere FS1-MGS8 (b).

Figure 8 Diffuse reflection Fourier transform infrared spectrum of FS1-MGS8 from 3000 cm^{-1} to 4000 cm^{-1}.

Figure 9 Types of silanol groups and siloxane bridge on the surface of FS1-MGS8. (a) Isolated silanol groups, (b) Genimal silanol groups.

Figure 10 Silanol content in FS1-MGS8 after calcination at 600 ~ 1100 °C.

Figure 11 Equilibrium adsorption isotherm of methylene blue onto FS1-MGS8 at room temperature.

Figure 12 Fitting of methylene blue adsorption onto FS1-MGS8 data to the kinetic models. (a) Pseudo first-order and pseudo second-order models, (b) Weber & Morris model.

Figure 13 FTIR spectrum of FS1-MGS8 before and after methylene blue adsorption.

Figure 14 The proposed mechanisms for methylene blue adsorption onto FS1-MGS8. (a) Electrostatic interaction; (b) hydrogen-bonding.

(a)

20 nm

(b)

20 nm

3728

3705 3627

3597

Wave Numbers (cm^{-1})

(a)

(b)

siloxane bridge

(a)

(b)